# Charging time and loss optimization for LiNMC and LiFePO$_4$ batteries based on equivalent circuit models

CrossMark

Xiaosong Hu [a,b,*], Shengbo Li [a,c], Huei Peng [a,c], Fengchun Sun [b]

[a] Department of Mechanical Engineering, The University of Michigan, Ann Arbor, MI 48109, USA
[b] National Engineering Laboratory for Electric Vehicles, Beijing Institute of Technology, Beijing 100081, China
[c] State Key Laboratory of Automotive Safety and Energy, Tsinghua University, Beijing 100084, China

## HIGHLIGHTS

- Dual-objective optimal charging strategy for Li-ion battery is studied.
- Charging time and charging energy loss are optimally traded off.
- Impacts of battery charging voltage threshold, temperature, and aging are analyzed.
- Optimized battery models of two types of Li-ion batteries are used.
- Comparison with charging based on simpler and less accurate models is made.

## ARTICLE INFO

## ABSTRACT

Battery management system monitors and mitigates the operation of battery cells and stacks and is important for battery safety and reliability. This paper presents a dual-objective optimal charging strategy for two types of Li-ion batteries, which considers the conflict objectives of charging time and charging loss. The battery models developed in a prior research are used in the charging optimization. The influences of the charging voltage threshold, temperature, and health status on the charging results are analyzed for both lithium nickel–manganese–cobalt oxide (LiNMC) and lithium iron phosphate (LiFePO$_4$) batteries. A comparison with the charging results based on the models that cannot describe the entire battery dynamics is also performed.

© 2013 Elsevier B.V. All rights reserved.

## 1. Introduction

Depleting fossil fuel supply and increasing regulations on greenhouse gases continue to pressure the automotive industry to transition toward more sustainable energy sources [1–3]. Battery electric vehicles (BEVs) and plug-in hybrid electric vehicles (PHEVs) are being actively developed for near-term production. The global annual sale of light-duty BEVs/PHEVs is projected to be more than 100 million by 2050 [4]. Compared to refueling of conventional internal-combustion-engine (ICE)-based vehicles, battery charging is slower and needs more careful consideration and management [5–8]. Recharging time is a serious concern for drivers, since it affects the convenience of vehicle usage. On the other hand, the PHEV/

BEV can stress the grid if charging is left unmitigated [9–11]. In addition, charging energy loss can also be a factor to be considered.

The most widely used charging scheme for Li-ion batteries is constant-current constant-voltage (CCCV) [12,13]. In the CC phase, the charging current is kept constant until the specified voltage threshold is reached. The charging process then switches to the CV phase, in which the charging voltage is maintained until the charging rate is below a certain threshold. This approach is simple and easy to implement, but it is open-loop in nature and does not explicitly take charging time or charging loss into account.

More complex charging strategies have been suggested based on fuzzy logic [14–16], neural networks [17], grey system theory [18]. genetic algorithm [19], and ant-colony system algorithm [20]. Although this type of computationally intelligent techniques could achieve faster charging, an explicit optimization problem for minimizing charging time was not considered. Furthermore, some of them require laborious tuning [21]. A nonlinear model predictive control problem was formulated to minimize charging time of a

* Corresponding author. No. 5 South Zhongguancun Street, Haidian District, Beijing 100081, China. Tel./fax: +86 10 6891 4625.
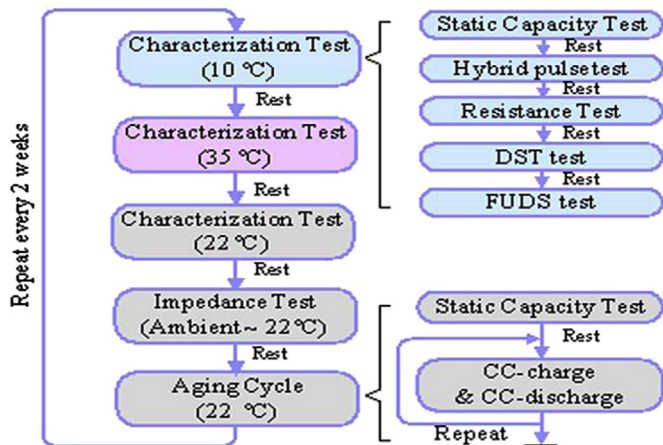E-mail addresses: huxstank@bit.edu.cn, huxiaos@umich.edu (X. Hu).

**Fig. 1.** The test schedule used to collect battery data.

Li-ion battery, given an electrochemical model [22]. Since the electrochemical model characterizes dynamics of internal states of the battery, constraints on side reactions at the anode and the cathode can be considered in the minimum-time control strategy. By using a shorter optimization horizon, the computation time is reduced, but the model complexity does not change. A major challenge is the identification of a large number of model parameters and acquiring state measurements or estimations. In addition, in this algorithm, the battery voltage is allowed to exceed the upper cut-off voltage for extended period of time, which may have practical safety implication. We believe less aggressive charging strategy must be developed.

Charging profiles can also be manipulated to minimize charging loss based on equivalent circuit battery models. In Refs. [23], based on a second-order equivalent circuit model, the optimal current profile was solved to maximize energy saving during charging a lithium iron phosphate battery, given a fixed charging duration, and its superiority to CCCV was demonstrated.

To our best knowledge, no algorithm that balances between charging time and loss has been published. These two goals are naturally in conflict due to the fact ohmic loss dominates charging losses. These two conflicting goals can also be interpreted as tradeoff between convenience to the PHEV owners and stress to the grid. It is thus valuable to study how to optimize this tradeoff. In this paper we treat charging time and loss as two conflicting objectives and then formulate a multi-objective optimal charging control problem, and apply it to two types of Li-ion batteries. The battery models developed in our earlier work [24,25] are used. The effect of the battery voltage threshold, temperature, and health status on the charging algorithm is analyzed. A comparison with the charging algorithms using less accurate models is also conducted.

The remainder of this paper is structured as follows. In Section 2, the Li-ion battery data set and the battery models are described. In Section 3, the multi-objective optimal charging control problem is formulated, and the pseudospectral technique is used to solve the problem. The impacts of the battery voltage threshold, temperature, and health status on the charging optimization results are discussed in Section 4, where a comparison with the charging algorithms using less accurate models is also given. Finally, conclusions are presented in Section 5.

## 2. Li-ion battery testing and modeling

Lithium nickel−manganese−cobalt oxide (LiNMC) UR14650P and lithium iron phosphate (LiFePO$_4$) APR18650M1A cells (8 cells
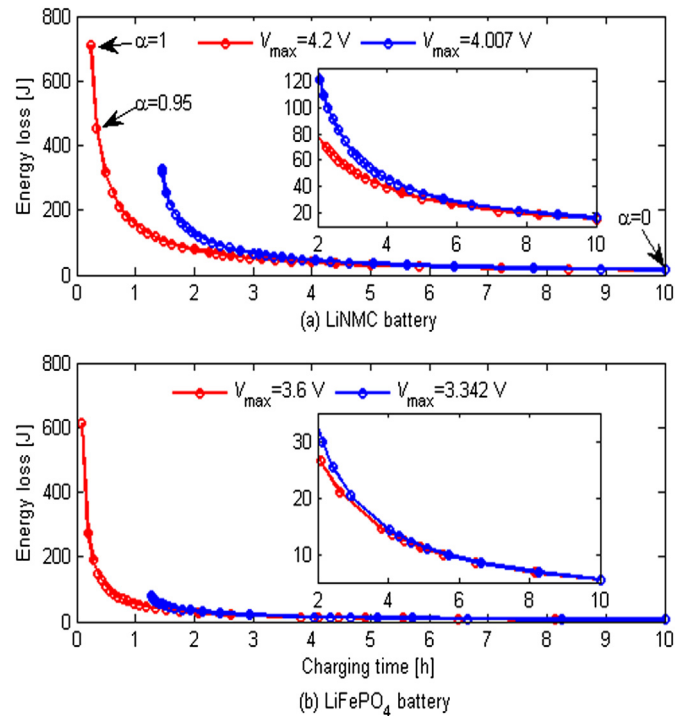


**Fig. 2.** Pareto charts of the multi-objective optimization for the two types of Li-ion batteries at 22 °C: (a) LiNMC battery; (b) LiFePO$_4$ battery.

each) were tested using the schedules shown in Fig. 1. In each schedule, it begins with a characterization test under temperature $T = 10$ °C based on the Arbin tester, followed by two identical characterization tests conducted under other temperatures $T = 35$ °C and $T = 22$ °C. A static capacity test, a hybrid pulse test, a dc resistance test, a DST test, and a FUDS test are consecutively conducted in each characterization test. After these characterization tests, an impedance test is conducted by means of the impedance tester which can collect data for battery impedance spectrum analysis. Then, the degradation test comprising a static
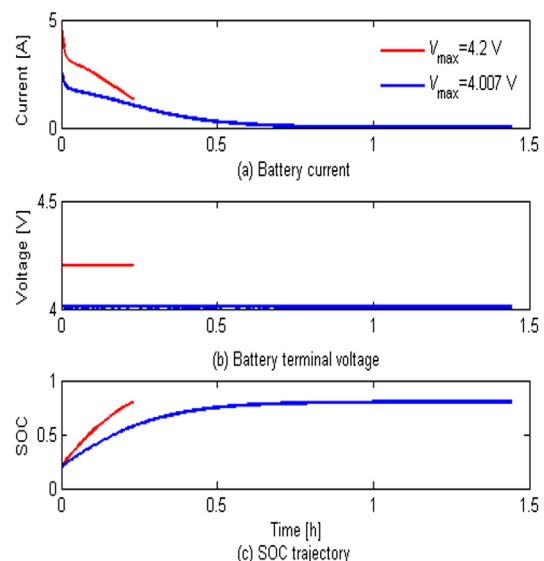


**Fig. 3.** LiNMC battery current, voltage, and SOC for minimum charging time at 22 °C.

**Table 4**
Minimum energy losses for LiNMC and LiFePO₄ batteries charging.

| | LiNMC | | | LiFePO₄ | | |
|---|---|---|---|---|---|---|
| | 1.44 h | 3 h | 10 h | 1.44 h | 3 h | 10 h |
| OCV at 80% SOC [%] | 4.23 | 0.89 | 0.22 | 0.77 | 0.28 | 0.08 |
| Upper cut-off voltage [%] | 1.44 | 0.70 | 0.21 | 0.55 | 0.26 | 0.079 |
| Improvement [%] | 323.00 | 27.14 | 4.76 | 40.00 | 7.69 | 1.27 |

**Table 5**
Minimum charging times for the two batteries under the three temperatures.

| Temperature [°C] | Minimum charging time [min] | | Time increase [%] | |
|---|---|---|---|---|
| | LiNMC | LiFePO₄ | LiNMC | LiFePO₄ |
| 10 | 16.02 | 7.26 | 31.64 | 80.15 |
| 22 | 13.85 | 5.20 | 13.80 | 29.03 |
| 35 | 12.17 | 4.03 | – | – |

capacity measure and aging cycles is conducted under temperature $T = 22$ °C until the experimental procedure ends. Repeat the experimental schedule until all the cells fail. The testing facility, procedure, and sampled datasets are detailed in Refs. [24], where the three dynamic test cycles (Hybrid pulse, DST, and FUDS) were used to identify the best model templates for the two types of batteries. Considering model complexity, training and validation accuracies based on test data from multiple cells, twelve commonly used equivalent circuit battery models in the literature were compared, and the first-order resistance-capacitance (RC) model and the first-order RC model with one-state hysteresis were found to be the best choice for LiNMC and LiFePO₄ cells, respectively [24]. In Refs. [25], the parameter dependence on the battery SOC and temperature were presented, and the established models were verified to have an average RMS (root-mean-square) voltage error of around 5 mV, leading to accurate SOC estimates under different loading and temperature conditions. The equations and detailed parameters of the two models for the LiNMC and LiFePO₄ batteries are given in Tables 1, 2, and 3 (see the Appendix), respectively. The physical meanings of the model parameters are also given in Table 1.

## 3. Dual-objective optimization formulation

Given the battery models shown in Tables 1–3, the power consumption is calculated from
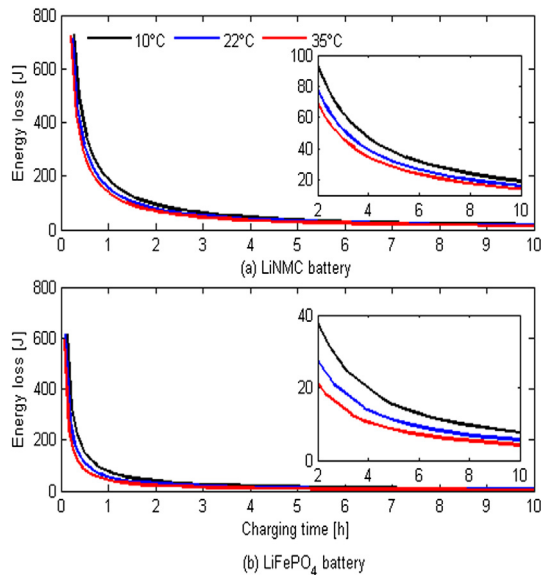
$$P_{loss} = I^2 R_0 + \frac{U^2}{R_1}. \tag{1}$$

If $\boldsymbol{x}$ denotes the state vector of the battery model, Eq. (1) can be rewritten as

$$P_{loss} = R_0 I^2 + \boldsymbol{x}^T \boldsymbol{Q} \boldsymbol{x}, \tag{2}$$

where for the LiNMC battery, we have

$$\boldsymbol{x} = [z \quad U]^T$$
$$\boldsymbol{Q} = \begin{bmatrix} 0 & 0 \\ 0 & \frac{1}{R_1} \end{bmatrix}; \tag{3}$$

and for the LiFePO₄ battery,

$$\boldsymbol{x} = [z \quad U \quad h]^T$$
$$\boldsymbol{Q} = \begin{bmatrix} 0 & 0 & 0 \\ 0 & \frac{1}{R_1} & 0 \\ 0 & 0 & 0 \end{bmatrix}. \tag{4}$$

The cost function of the multi-objective optimal control problem for minimizing charging time and energy loss is then defined as

$$J = \alpha t_f M + (1 - \alpha) \int_0^{t_f} P_{loss} dt, \tag{5}$$

where $t_f$ is the charging time, $0 \leq \alpha \leq 1$ is the weighting factor to reflect the relative importance of the two objectives, and $M$ is a



**Fig. 4.** Pareto charts for the dual-objective optimization under the three temperatures: (a) LiNMC battery; (b) LiFePO₄ battery.
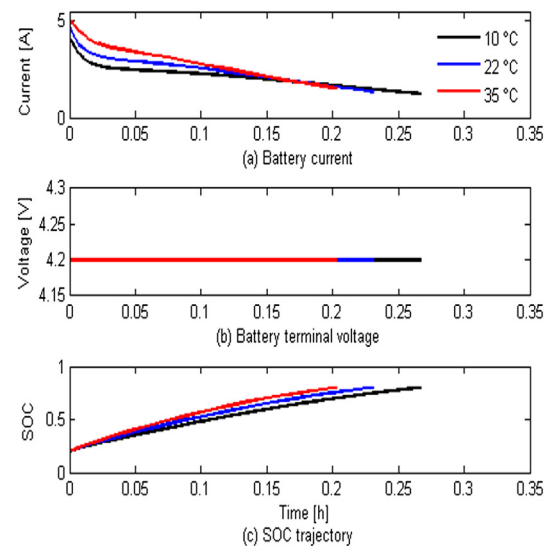


**Fig. 5.** LiNMC battery current, voltage, and SOC in the charging-time minimizations under the three temperatures.

**Table 6**
Charging times for the compromise points ($\alpha = 0.5$, balanced charging) of the two batteries under the three temperatures.

| Temperature [°C] | Charging time [min] | | Time increase [%] | |
|---|---|---|---|---|
| | LiNMC | LiFePO$_4$ | LiNMC | LiFePO$_4$ |
| 10 | 96.42 | 61.56 | 16.28 | 35.59 |
| 22 | 88.08 | 52.15 | 6.22 | 14.87 |
| 35 | 82.92 | 45.40 | – | – |

**Table 8**
Minimum energy losses during the two batteries charging under the three temperatures.

| Temperature [°C] | Energy loss [%] | | Loss increase [%] | |
|---|---|---|---|---|
| | LiNMC | LiFePO$_4$ | LiNMC | LiFePO$_4$ |
| 10 | 0.25 | 0.12 | 38.89 | 100.00 |
| 22 | 0.21 | 0.08 | 16.67 | 33.33 |
| 35 | 0.18 | 0.06 | – | – |

scaling constant to ensure the two objectives have similar orders of magnitude. The optimization problem is subject to the following constraints:

$$\boldsymbol{F}\left(\frac{\mathrm{d}\boldsymbol{x}}{\mathrm{d}t}, \boldsymbol{x}, t\right) = 0, \tag{6}$$

$$z(0) = 20\%, \tag{7}$$

$$z\left(t_f\right) = 80\%, \tag{8}$$

$$0 \le I \le I_{\max}, \tag{9}$$

$$V \le V_{\max}, \tag{10}$$

$$0 \le t_f \le t_{\max}, \tag{11}$$

where $\boldsymbol{F}(.)$ denotes the state equations shown in Table 1. $t_{\max}$, $I_{\max}$, and $V_{\max}$ are the maximum charging time, maximum current, and maximum charging voltage, respectively. The SOC of the battery packs is limited because of life consideration [26–29]. The upper limit of $t_{\max}$ is set to 10 h which is selected to allow for Level I charging [5,30].

Since the model parameters vary with SOC and temperature (see Tables 2 and 3), the optimization method must work with nonlinear and time-varying dynamics. The pseudo-spectral technique was shown to solve complicated nonlinear optimal control problems [31–34], including aerospace and autonomous flight systems [35,36] and ground vehicle control systems [23,37]. The pseudo-spectral method discretizes the dynamics to form a nonlinear programming (NLP) problem that can be efficiently solved by sparse NLP tools. There are different approaches to implementing the discrete approximations of the state equations and the cost function, leading to many pseudo-spectral variants. We use the general purpose optimal control software (GPOPS-II) [38], which includes the advanced Radau Pseudo-spectral Method (RPM) solver. The RPM is an orthogonal collocation method to generate Legendre–Gauss–Radau points for good approximation accuracy. The novel $hp$-adaptive mesh refinement algorithm is selected to iteratively adjust the number of mesh intervals, the width of intervals, and the polynomial degree in each interval to

reduce the approximation error. Details of RPM and the $hp$-adaptive algorithm can be found in Refs. [39–44]. The large-scale spare NLP solver, SNOPT [45], based on the sequential quadratic programming (SQP) algorithm, is used to solve the transcribed NLP problem. Because the purpose of the paper is not to characterize the transient battery thermal behavior, we assume that an effective thermal management system is available to maintain the battery temperature approximately constant during charging.

## 4. Results and discussion

### 4.1. Impact of the maximum charging voltage $V_{max}$

The maximum charging voltage $V_{\max}$ must be larger than the OCV at the SOC target, and less than the cut-off voltage to avoid overcharging. Here we study how $V_{\max}$ affects the multi-objective charging optimization.

The Pareto charts of the multi-objective optimization for the two types of Li-ion batteries at 22 °C are plotted in Fig. 2. It is clear that the charging time and charging loss are conflicting goals. Compared to the case of using the OCV at 80% SOC (i.e., 4.007 V for the LiNMC battery and 3.342 V for the LiFePO$_4$ battery) as the voltage limit, a smaller charging time is obtained when using the upper cut-off voltage (i.e., 4.2 V for the LiNMC battery and 3.6 V for the LiFePO$_4$ battery). The optimized LiNMC battery current, voltage, and SOC for minimum charging time are shown in Fig. 3. It is observed that the smaller $V_{\max}$ slows the charging rate down, but achieves lower losses. The minimum percent losses for three
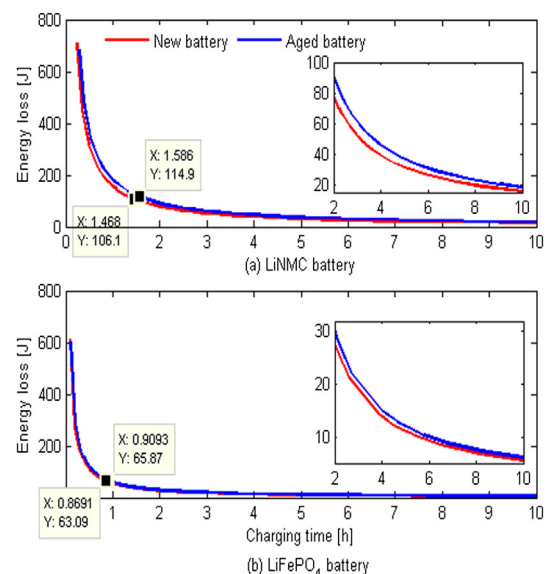
**Table 7**
Energy losses for the compromise points ($\alpha = 0.5$, balanced charging) of the two batteries under the three temperatures.

| Temperature [°C] | Energy loss [%] | | Loss increase [%] | |
|---|---|---|---|---|
| | LiNMC | LiFePO$_4$ | LiNMC | LiFePO$_4$ |
| 10 | 1.55 | 1.13 | 18.32 | 43.04 |
| 22 | 1.41 | 0.93 | 7.63 | 17.72 |
| 35 | 1.31 | 0.79 | – | – |



**Fig. 6.** Pareto charts for the LiNMC and LiFePO$_4$ battery at different aging levels.

**Table 9**
Comparison of the algorithm from the new battery and the optimal charging algorithm used to the aged battery.

| | LiNMC | | LiFePO$_4$ | |
|---|---|---|---|---|
| | Time [min] (decrease [%]) | Loss [%] (increase [%]) | Time | Loss |
| Algorithm from the new battery | 82.20 (13.84) | 1.90 (15.85) | 51.00 (6.59) | 1.03 (6.19) |
| Optimal | 95.40 | 1.64 | 54.60 | 0.97 |

example charging times are shown in Table 4. It is apparent that using the upper cut-off voltage to charge the battery reduces charging loss, especially when the charging time is relatively short. The upper cut-off voltage is thereby used in the following sections.

### 4.2. Impact of battery temperature during charging

The battery models optimized in Refs. [24,25] take different temperatures (10 °C, 22 °C, and 35 °C) into account, which enables us to quantify how the temperature influences the dual-objective charging optimization.

The Pareto curves of the dual-objective optimization for the LiNMC and LiFePO$_4$ batteries under three temperatures are shown in Fig. 4. Different values of $\alpha$ between 0 and 1 are used to generate the Pareto curve. As the temperature reduces, the Pareto curve moves to the top right − both the optimized charging time and energy loss degenerate. The degradation is relatively large when the charging time ranges from 1 to 4 h. A closer examination on the three points corresponding to the weight values of 1, 0.5, and 0 is conducted. The minimum charging times ($\alpha = 1$, fast charge) under the three temperatures are shown in Table 5. The associated LiNMC battery current, voltage, and SOC are shown in Fig. 5. Because of the smaller resistance, the charging current starting the CV stage at 35 °C is higher, resulting in a shorter charging time. The charging times for the balanced charging ($\alpha = 0.5$) under three temperatures are shown in Table 6, while the energy losses are shown in Table 7. It is clear that the lower the temperature, the larger the charging time and energy loss. Minimum energy losses ($\alpha = 0$, 10-h slow charge) under the three temperatures are shown in Table 8. The lowest energy loss occurs at 35 °C. It can be concluded that a higher (but still safe) temperature is preferred to optimally tradeoff between charging time and energy loss.

### 4.3. Impact of battery age

Li-ion batteries irreversibly degrade in real-word use − the battery capacity and power delivery capability fade, as the cycle number increases. The degradation has a large impact on the battery dynamics, thus altering charging characteristics of the battery. Here, without loss of generality, we take the battery aging at 22 °C as an example to illustrate its impact on the multi-objective optimization results.
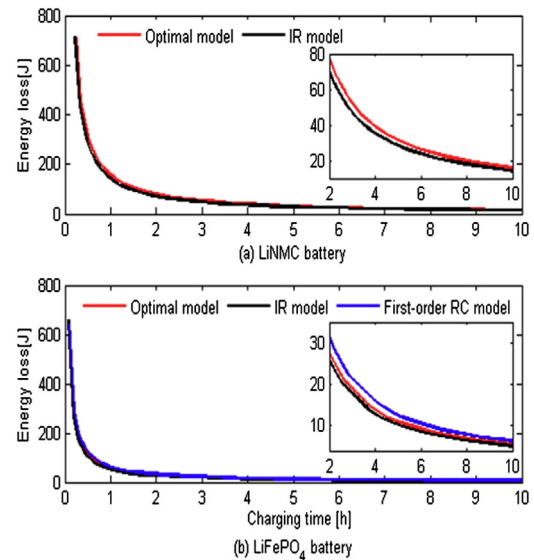


**Fig. 7.** Comparison of Pareto charts: (a) LiNMC battery; (b) LiFePO$_4$ battery.

The aging level up to cell age of 342 cycles for the LiNMC battery at 22 °C is considered, and the hybrid pulse test data right after 342 cycles is employed to update all the parameters of the LiNMC battery model, as done in Ref. [25]. We have finished 2600 cycles for LiFePO$_4$ cells, and the capacity loss at 22 °C is only around 3%. The aging level up to 2587 cycles is chosen. The Pareto curves for the new and aged LiNMC and LiFePO$_4$ batteries at 22 °C are shown in Fig. 6. It can be seen that as the battery ages, both the charging time and energy loss increase. From the two compromise points, we can clearly see the aging effect on the charging optimization. The charging results are shown in Table 9 when we use the charging algorithm optimized for the new battery ($\alpha = 0.5$) to the aged battery. Compared to the optimal tradeoff, the charging time is reduced, but the energy loss increases. Compared to the LiNMC battery, the difference between the two algorithms for the LiFePO$_4$ battery is minor, due to relatively small aging. To accomplish the optimal charging control, the charging current should be recalibrated when the battery degrades. Otherwise, it would cause a non-optimal charging control with a larger energy loss.

Further, we compare CCCV and the optimal charging algorithm with battery aging. Suppose that the charging time desired by the user is 1 h, and the CCCV algorithm does not consider or compensate for battery aging, the battery will be fully charged sooner and result in higher loss. The comparison results for the two types of Li-ion batteries are shown in Table 10.

### 4.4. Comparison with charging algorithms using simpler models

The charging results reported above are all based on the models shown in Tables 1–3. Natural questions to ask are

**Table 10**
Comparison of CCCV and optimal charging algorithm in the battery aging context.

| | LiNMC | | | | LiFePO$_4$ | | | |
|---|---|---|---|---|---|---|---|---|
| | New | | Aged | | New | | Aged | |
| | Time [min] (decrease [%]) | Loss [%] (increase [%]) | Time | Loss | Time | Loss | Time | Loss |
| CCCV | 60.00 (−) | 2.07 (0.49) | 55.80 (7) | 2.76 (7.81) | 60.00 (−) | 0.79 (1.28) | 58.20 (3) | 0.90 (3.45) |
| Optimal | 60.00 | 2.06 | 60.00 | 2.56 | 60.00 | 0.78 | 60.00 | 0.87 |

**Table 11**
Tradeoff comparison of the LiNMC battery with different charging algorithms at the compromise point.

| | Time [min] (change [%]) | Loss [%] (change [%]) |
|---|---|---|
| IR model-based charging | 83.91 (−4.73) | 1.48 (+4.96) |
| RC-model charging (optimal tradeoff) | 88.08 | 1.41 |

**Table 12**
Tradeoff comparison of the LiFePO$_4$ battery with different charging algorithms at the compromise point.

| | Time [min] (change [%]) | Loss [%] (change [%]) |
|---|---|---|
| IR model-based charging | 50.74 (−2.70) | 0.94 (+4.44) |
| RC model-based charging | 55.23 (+5.91) | 0.86 (−4.44) |
| RC-plus hysteresis model charging (optimal tradeoff) | 52.15 | 0.90 |

whether it is necessary to use the RC- and RC-plus-hysteresis models, and whether simpler model will yield similar charging strategy and insights. In the following, the internal resistance (IR) model is considered for the LiNMC battery (without RC), while the first-order RC model for the LiFePO$_4$ battery (without hysteresis). The dependency of these models on the SOC and temperature is described by the same function structures as shown in Tables 2 and 3, and the function coefficients are identified by using the optimization method in Ref. [25]. The comparison results at 22 °C are shown in Fig. 7. It is clear that the Pareto chart of the IR model moves to the lower left, indicating a smaller charging time and energy loss. This seemingly better result is because the IR model cannot characterize the relaxation dynamics of the battery. Therefore, a smaller resistance $R_0$ is identified, compared to the total resistance ($R_0 + R_1$) in the optimal model (the current flowing through $R_1$ in the RC network is smaller than that for $R_0$). For the LiFePO$_4$ battery, the Pareto chart of the first-order model moves to the up right. This pessimistic result is because the lack of the hysteresis voltage results in a higher identified total resistance ($R_0 + R_1$) in the first-order RC model than that in the optimal model. Further, we apply the charging algorithm identified from the simpler model to the "real battery" which is represented by the RC or RC-plus-hysteresis model and investigate the impact on the optimal tradeoff between the charging time and loss. The results for the LiNMC and LiFePO$_4$ batteries at the compromise points ($\alpha = 0.5$) are shown in Tables 11 and 12, respectively. It can be seen that the charging algorithm from the IR model reduces the charging time but increases the energy loss, whereas that from the RC model for the LiFePO$_4$ battery decreases the energy loss but has a longer charging time. Both cases lead to a non-optimal tradeoff between the two conflicting objectives for the specified weight $\alpha$. It can be observed that the charging deteriorations for both the IR- and RC-model algorithms are however small. These simpler models may provide acceptable charging optimization results when the computational capability of charge controller is low.

## 5. Conclusions

A multi-objective optimal charging control problem is formulated for two types of Li-ion batteries to optimally tradeoff the conflict between the charging time and energy loss. Based on the optimal battery models for the LiNMC and LiFePO$_4$ cells developed in Refs. [24,25], the advanced Radau Pseudo-spectral Method (RPM), together with the adaptive $hp$-adaptive mesh refinement algorithm, is used to solve the optimal control problem. The impacts of the battery voltage threshold, temperature, and health status on the optimization results are investigated in detail. We found that the use of the upper cut-off voltage to limit the battery voltage during charging in PEVs applications benefits in minimizing the charging time and energy loss. The analysis of the optimal charging under three different temperatures shows that a relatively high (but still safe) temperature permitted by thermal management system is preferred to optimally tradeoff the charging time and energy loss, due to a smaller battery resistance. The temperature has a relatively large influence in moderate-charge case. As the battery ages, both the optimized charging time and energy loss become larger, leading to a deteriorated balance between the two objectives. In order to achieve an optimal charging control, the charging current profile should be recalibrated when the battery fades. Compared to CCCV, the optimal algorithm has an obvious energy-saving advantage in the battery aging context. The LiFePO$_4$ battery can provide a better tradeoff between the two conflicting objectives than the LiNMC battery, owing to a much smaller resistance. A comparison with Pareto charts (charging tradeoffs) calculated using less accurate models verifies that it is advantageous to use the RC- and RC-plus-hysteresis models to simulate the real LiNMC and LiFePO$_4$ batteries, respectively. The results of employing simpler-model identified charging control on the "real battery" (emulated by the RC- or RC-plus-hysteresis model) illustrate that both the IR- and RC-model algorithms (IR for the LiNMC battery, IR and RC for the LiFePO$_4$ battery) lead to a non-optimal tradeoff between the charging time and loss for a specified weight $\alpha$. The consequent charging-tradeoff deterioration is, however, relatively small, which might be acceptable when the computational and storage capability of the model-based charge controller is limited.

## Appendix

**Table 1**
Equations of the best performing models identified in Refs. [24,25].

| Model | Equations |
|---|---|
| (1) First-order RC model for LiNMC cell | $\begin{cases} \dfrac{dz(t)}{dt} = \dfrac{\eta I(t)}{3600 C_n} \\ \dfrac{dU(t)}{dt} = \dfrac{-U(t)}{\tau_1} + \dfrac{R_1}{\tau_1} I(t) \end{cases}$, $V(t) = V_{oc}(z(t)) + R_0 I(t) + U(t)$ where $I, V, C_n$, and $z$ are the current, output voltage, nominal capacity, and SOC, respectively. $\eta$ is Coulombic efficiency, $V_{oc}$ is the open circuit voltage, and $R_0$ is the internal ohmic resistance that depends on the current direction. $U$ and $\tau_1 = R_1 C_1$ are the voltage and time constant of the RC network. |
| (2) First-order RC model with one-state hysteresis for LiFePO$_4$ cell | $\begin{cases} \dfrac{dz(t)}{dt} = \dfrac{\eta I(t)}{3600 C_n} \\ \dfrac{dU(t)}{dt} = \dfrac{-U(t)}{\tau_1} + \dfrac{R_1}{\tau_1} I(t) \\ \dfrac{dh(t)}{dt} = -|\kappa I(t)| h(t) + |\kappa I(t)| H \end{cases}$, $V(t) = V_{oc}(z(t)) + R_0 I(t) + U(t) + h(t)$ where $h$ is the hysteresis voltage, $\kappa$ is a decaying factor, and $H$ is the maximum amount of hysteresis voltage that is positive for charge and negative for discharge. |

**Table 2**
Model parameters for the LiNMC cell [25].

| Parameter | Coefficients |
|---|---|
| OCV | $V_{oc} = \alpha_1 z^6 + \alpha_2 z^5 + \alpha_3 z^4 + \alpha_4 z^3 + \alpha_5 z^2 + \alpha_6 z + \alpha_7$ $(0.1 \leq z \leq 0.9)$<br>where<br>$\alpha_1 = \left\{ -0.1674(Te-10) + 2.9192, 10 \leq Te < 22 \ (Te: \text{Temperature}), 0.1939(Te-22) + 0.9109, 22 \leq Te \leq 35 \right\}$,<br>$\alpha_2 = \left\{ 0.3394(Te-10) - 5.8608, 10 \leq Te < 22, -0.3675(Te-22) - 1.7875, 22 \leq Te \leq 35 \right\}$, $\alpha_3 = \left\{ -0.1811(Te-10) + 1.3408, 10 \leq Te < 22, 0.0469(Te-22) - 0.8330, 22 \leq Te \leq 35 \right\}$,<br>$\alpha_4 = \left\{ -0.0614(Te-10) + 5.1684, 10 \leq Te < 22, 0.3023(Te-22) + 4.4320, 22 \leq Te \leq 35 \right\}$, $\alpha_5 = \left\{ 0.0948(Te-10) - 4.4983, 10 \leq Te < 22, -0.2336(Te-22) - 3.3606, 22 \leq Te \leq 35 \right\}$,<br>$\alpha_6 = \left\{ -0.0290(Te-10) + 1.5815, 10 \leq Te < 22, 0.0648(Te-22) + 1.2331, 22 \leq Te \leq 35 \right\}$, $\alpha_7 = \left\{ 0.0025(Te-10) + 3.5600, 10 \leq Te < 22, -0.0063(Te-22) + 3.5901, 22 \leq Te \leq 35 \right\}$. |
| Charging $R_0$ | $R_0 = c_1 e^{-c_2 z} + c_3$ $(0.1 \leq z \leq 0.9)$<br>where<br>$c_1 = \left\{ -0.0116(Te-10) + 0.1728, 10 \leq Te < 22, 0.0741(Te-22) + 0.0337, 22 \leq Te \leq 35 \right\}$, $c_2 = \left\{ 0.5632(Te-10) - 24.5426, 10 \leq Te < 22, -1.0925(Te-22) - 17.7848, 22 \leq Te \leq 35 \right\}$,<br>$c_3 = \left\{ -0.0009(Te-10) + 0.1086, 10 \leq Te < 22, -0.0005(Te-22) + 0.0972, 22 \leq Te \leq 35 \right\}$. |
| $R_1$ (RC network) | $R_1 = c_1 e^{-c_2 z} + c_3$ $(0.1 \leq z \leq 0.9)$<br>where<br>$c_1 = \left\{ 0, 10 \leq Te < 22, 0, 22 \leq Te \leq 35 \right\}$, $c_2 = \left\{ -0.1403(Te-10) - 21.9590, 10 \leq Te < 22, -0.6098(Te-22) - 23.6430, 22 \leq Te \leq 35 \right\}$,<br>$c_3 = \left\{ -0.0015(Te-10) + 0.0608, 10 \leq Te < 22, -0.0011(Te-22) + 0.0433, 22 \leq Te \leq 35 \right\}$. |
| Time constant $\tau_1$ (RC network) | $\tau_1 = c_1 e^{-c_2 z} + c_3$ $(0.1 \leq z \leq 0.9)$<br>where<br>$c_1 = \left\{ 2.1871(Te-10) + 19.3967, 10 \leq Te < 22, -1.9460(Te-22) + 45.6424, 22 \leq Te \leq 35 \right\}$, $c_2 = \left\{ -4.1106(Te-10) - 0.6723, 10 \leq Te < 22, 1.9550(Te-22) - 50.0000, 22 \leq Te \leq 35 \right\}$,<br>$c_3 = \left\{ 0.5091(Te-10) + 32.7608, 10 \leq Te < 22, 1.7591(Te-22) + 38.8700, 22 \leq Te \leq 35 \right\}$. |

**Table 3**
Model parameters for the LiFePO$_4$ cell [25].

| Parameter | Coefficients |
|---|---|
| OCV | $V_{oc} = \alpha_1 z^6 + \alpha_2 z^5 + \alpha_3 z^4 + \alpha_4 z^3 + \alpha_5 z^2 + \alpha_6 z + \alpha_7$  (0.1 ≤ z ≤ 0.9) <br> where <br> $\alpha_1 = \left\{ -0.4629(Te-10) + 1.9754, 10 \le Te < 22, 0.2506(Te-22) - 3.5795, 22 \le Te \le 35 \right\}$, $\alpha_2 = \left\{ 1.0943(Te-10) - 3.6280, 10 \le Te < 22, -0.7233(Te-22) + 9.5106, 22 \le Te \le 35 \right\}$, <br> $\alpha_3 = \left\{ -0.8341(Te-10) + 0.0094, 10 \le Te < 22, 0.8529(Te-22) - 10.0000, 22 \le Te \le 35 \right\}$, $\alpha_4 = \left\{ 0.1023(Te-10) + 4.3001, 10 \le Te < 22, -0.4813(Te-22) + 5.5273, 22 \le Te \le 35 \right\}$, <br> $\alpha_5 = \left\{ 0.1514(Te-10) - 3.7275, 10 \le Te < 22, 0.1121(Te-22) - 1.9108, 22 \le Te \le 35 \right\}$, $\alpha_6 = \left\{ -0.0631(Te-10) + 1.3896, 10 \le Te < 22, -0.0049(Te-22) + 0.6326, 22 \le Te \le 35 \right\}$, <br> $\alpha_7 = \left\{ 0.0068(Te-10) + 3.0629, 10 \le Te < 22, -0.0002(Te-22) + 3.1440, 22 \le Te \le 35 \right\}$. |
| Charging $R_0$ | $R_0 = c_1 z^3 + c_2 z^2 + c_3 z + c_4$  (0.1 ≤ z ≤ 0.9) <br> where <br> $c_1 = \left\{ 0.0148(Te-10) - 0.1670, 10 \le Te < 22, -0.0018(Te-22) + 0.0105, 22 \le Te \le 35 \right\}$, $c_2 = \left\{ -0.0221(Te-10) + 0.2458, 10 \le Te < 22, 0.0027(Te-22) - 0.0200, 22 \le Te \le 35 \right\}$, <br> $c_3 = \left\{ 0.0098(Te-10) - 0.1027, 10 \le Te < 22, -0.0014(Te-22) + 0.0149, 22 \le Te \le 35 \right\}$, $c_4 = \left\{ -0.0016(Te-10) + 0.0349, 10 \le Te < 22, -0.0001(Te-22) + 0.0151, 22 \le Te \le 35 \right\}$. |
| $R_1$ (RC network) | $R_1 = c_1 z^3 + c_2 z^2 + c_3 z + c_4$  (0.1 ≤ z ≤ 0.9) <br> where <br> $c_1 = \left\{ 0.0272(Te-10) - 0.3042, 10 \le Te < 22, -0.0058(Te-22) + 0.0220, 22 \le Te \le 35 \right\}$, $c_2 = \left\{ -0.0424(Te-10) + 0.4777, 10 \le Te < 22, 0.0078(Te-22) - 0.0309, 22 \le Te \le 35 \right\}$, <br> $c_3 = \left\{ 0.0226(Te-10) - 0.2715, 10 \le Te < 22, -0.0022(Te-22) - 0.0000, 22 \le Te \le 35 \right\}$, $c_4 = \left\{ -0.0054(Te-10) + 0.0956, 10 \le Te < 22, -0.0007(Te-22) + 0.0311, 22 \le Te \le 35 \right\}$. |
| Time constant $\tau_1$ (RC network) | $\tau_1 = c_1 z^3 + c_2 z^2 + c_3 z + c_4$  (0.1 ≤ z ≤ 0.9) <br> where <br> $c_1 = \left\{ 0.1124(Te-10) - 4.3311, 10 \le Te < 22, -0.2546(Te-22) - 2.9824, 22 \le Te \le 35 \right\}$, $c_2 = \left\{ -0.4379(Te-10) + 1.1861, 10 \le Te < 22, -0.0584(Te-22) - 4.0682, 22 \le Te \le 35 \right\}$, <br> $c_3 = \left\{ 0.2447(Te-10) + 6.2657, 10 \le Te < 22, -1.4771(Te-22) + 9.2026, 22 \le Te \le 35 \right\}$, $c_4 = \left\{ -0.9800(Te-10) + 35.2236, 10 \le Te < 22, 0.5832(Te-22) + 23.4637, 22 \le Te \le 35 \right\}$. |
| Hysteresis decaying factor $\kappa$ | $\kappa = c_1 z^3 + c_2 z^2 + c_3 z + c_4$  (0.1 ≤ z ≤ 0.9) <br> where <br> $c_1 = \left\{ 0.0379(Te-10) - 0.5478, 10 \le Te < 22, 0.0243(Te-22) - 0.0925, 22 \le Te \le 35 \right\}$, $c_2 = \left\{ -0.0521(Te-10) + 0.7931, 10 \le Te < 22, -0.0339(Te-22) + 0.1675, 22 \le Te \le 35 \right\}$, <br> $c_3 = \left\{ 0.0188(Te-10) - 0.3157, 10 \le Te < 22, 0.0124(Te-22) - 0.0903, 22 \le Te \le 35 \right\}$, $c_4 = \left\{ -0.0015(Te-10) + 0.0410, 10 \le Te < 22, -0.0011(Te-22) + 0.0233, 22 \le Te \le 35 \right\}$. |
| Maximum charging hysteresis $H$ | $H = c_1 z^3 + c_2 z^2 + c_3 z + c_4$  (0.1 ≤ z ≤ 0.9) <br> where <br> $c_1 = \left\{ -0.0248(Te-10) + 0.9525, 10 \le Te < 22, -0.0725(Te-22) + 0.6554, 22 \le Te \le 35 \right\}$, $c_2 = \left\{ 0.0306(Te-10) - 1.3109, 10 \le Te < 22, 0.1021(Te-22) - 0.9440, 22 \le Te \le 35 \right\}$, <br> $c_3 = \left\{ -0.0085(Te-10) + 0.4424, 10 \le Te < 22, -0.0331(Te-22) + 0.3399, 22 \le Te \le 35 \right\}$, $c_4 = \left\{ -0.0005(Te-10) + 0.0060, 10 \le Te < 22, 0.0018(Te-22) + 0.0000, 22 \le Te \le 35 \right\}$. |

## References

[1] S. Chu, A. Majumdar, Nature 488 (2012) 294–303.
[2] T.R. Hawkins, O.M. Gausen, A.H. Strømman, Int. J. Life Cycle Assess. 17 (2012) 997–1014.
[3] A. Emadi, IEEE Power Energy Mag. 9 (2011) 18–29.
[4] International Energy Agency (IEA), Technology Roadmap: Electric and Plug-in Hybrid Electric Vehicles. Technical Report, IEA, Paris, France, 2011.
[5] M. Yilmaz, P.T. Krein, IEEE Trans. Power Electron. 28 (2013) 2151–2169.
[6] C.S. Ahn, C.T. Li, H. Peng, J. Power Sources 196 (2011) 10369–10379.
[7] D. Andrea, Battery Management Systems for Large Lithium-Ion Battery Packs, Artech House, Boston, 2010.
[8] K. Young, C. Wang, L. Wang, K. Strunz, in: R.G. Valle, J.A.P. Lopes (Eds.), Electric Vehicle Integration into Modern Power Networks, Springer, New York, 2013, pp. 15–56.
[9] S. Bashash, S.J. Moura, J.C. Forman, H.K. Fathy, J. Power Sources 196 (2011) 541–549.
[10] S. Bashash, S.J. Moura, H.K. Fathy, J. Power Sources 196 (2011) 8747–8754.
[11] Y. He, B. Venkatesh, L. Guan, IEEE Trans. Smart Grid 3 (2012) 1095–1105.
[12] S. Dearborn, Power Electron. Technol. 31 (2005) 40–49.
[13] S.S. Zhang, K. Xu, T.R. Jow, J. Power Sources 160 (2006) 1349–1354.
[14] G.C. Hsieh, L.R. Chen, K.S. Huang, IEEE Trans. Ind. Electron. 48 (2001) 585–593.
[15] Y.H. Liu, Y.F. Luo, IEEE Trans. Ind. Electron. 57 (2010) 3963–3971.
[16] Y.H. Liu, C.H. Hsieh, Y.F. Luo, IEEE Trans. Energy Convers. 26 (2011) 654–661.
[17] Z. Ullah, B. Burford, S. Dillip, Electron. Syst. Mag. 11 (1996) 26–34.
[18] L.R. Chen, R.C. Hsu, C.S. Liu, IEEE Trans. Ind. Electron. 55 (2008) 3692–3701.
[19] H. Surmann, IEEE Trans. Ind. Electron. 43 (1996) 541–548.
[20] Y.H. Liu, J.H. Teng, Y.C. Lin, IEEE Trans. Ind. Electron. 52 (2005) 1328–1336.
[21] L.R. Chen, S.L. Wu, T.R. Chen, W.R. Yang, C.S. Wang, P.C. Chen, Detecting of Optimal Li-Ion Battery Charging Frequency by Using AC Impedance Technique, in: The 4th IEEE Conference on Industrial Electronics and Applications (2009), pp. 3378–3381.
[22] R. Klein, N.A. Chaturvedi, J. Christensen, J. Ahmed, R. Findeisen, A. Kojic, Optimal Charging Strategies in Lithium-Ion Battery, in: American Control Conference (2011), pp. 382–387.
[23] E. Inoa, J. Wang, IEEE Trans. Veh. Technol. 60 (2011) 2978–2986.
[24] X. Hu, S. Li, H. Peng, J. Power Sources 198 (2012) 359–367.
[25] X. Hu, S. Li, H. Peng, F. Sun, J. Power Sources 217 (2012) 209–219.
[26] C. Mi, M.A. Masrur, D. Gao, Hybrid Electric Vehicles-Principles and Applications with Practical Perspectives, John Wiley & Sons, West Sussex, 2011.
[27] S.J. Moura, H.K. Fathy, D.S. Callaway, J.L. Stein, IEEE Trans. Control Syst. Technol. 19 (2011) 545–555.
[28] D. Kum, H. Peng, N.K. Bucknor, IEEE Trans. Control. Syst. Technol. 21 (2013) 14–26.
[29] M. Pourabdollah, V. Larsson, L. Johannesson, B. Egardt, PHEV Energy Management: A Comparison of Two Levels of Trip Information. SAE Technical Paper 2012-01-0745, SAE World Congress & Exhibition, Detroit, 2012.
[30] SAE Electric Vehicle and Plug-in Hybrid Electric Vehicle Conductive Charge Coupler (2010). SAE standard J1772.
[31] G. Elnagar, M.A. Kazemi, M. Razzaghi, IEEE Trans. Autom. Control 40 (1995) 1793–1796.
[32] F. Fahroo, I.M. Ross, J. Guid. Control Dynam. 31 (2008) 927–936.
[33] F. Fahroo, I.M. Ross, Advances in Pseudospectral Methods for Optimal Control, in: AIAA Paper 2008-7309, AIAA Guidance, Navigation and Control Conference (2008).
[34] Q. Gong, W. Kang, I.M. Ross, IEEE Trans. Autom. Control 51 (2006) 1115–1129.
[35] Q. Gong, W. Kang, N.S. Bedrossian, F. Fahroo, P. Sekhavat, K. Bollino, Pseudospectral Optimal Control for Military and Industrial Applications, in: The 46th IEEE Conference on Decision and Control (2007), pp. 4128–4142.
[36] I.M. Ross, M. Karpenko, Annu. Rev. Control 36 (2012) 182–197.
[37] S. Li, H. Peng, Proc. Inst. Mech. Eng. Pt. D J. Automobile Eng. 226 (2012) 419–429.
[38] GPOPS-II: Next-Generation Optimal Control Software, http://www.gpops.org/.
[39] A.V. Rao, D.A. Benson, C.L. Darby, M.A. Patterson, C. Francolin, I. Sanders, G.T. Huntington, ACM Trans. Math. Software 37 (2010).
[40] D.A. Benson, G.T. Huntington, T.P. Thorvaldsen, A.V. Rao, J. Guid. Control Dynam. 29 (2006) 1435–1440.
[41] D. Garg, M.A. Patterson, C.L. Darby, C. Francolin, G.T. Huntington, W.W. Hager, A.V. Rao, Comput. Optim. Appl. 49 (2011) 335–358.
[42] D. Garg, M.A. Patterson, W.W. Hager, A.V. Rao, D.A. Benson, G.T. Huntington, Automatica 46 (2010) 1843–1851.
[43] D. Garg, W.W. Hager, A.V. Rao, Automatica 47 (2011) 829–837.
[44] C.L. Darby, W.W. Hager, A.V. Rao, Optim. Contr. Appl. Met. 32 (2011) 476–502.
[45] P.E. Gill, W. Murray, M.A. Saunders, SIAM Rev. 47 (2005) 99–131.